CHINESE OPTICS LETTERS

Vol. 21, No. 8 | August 2023

Nonlinear harmonic generation of terahertz waves in a topological valley polaritonic microcavity

Yao Lu (卢 瑶)[1,2,†], Hao Xiong (熊 浩)[1,2,†], Yibo Huang (黄意博)[1,2], Qiang Wu (吴 强)[1,2*], Jiwei Qi (齐继伟)[1,2], Chongpei Pan (潘崇佩)[1,2**], and Jingjun Xu (许京军)[1,2]

[1] Key Laboratory of Weak-Light Nonlinear Photonics, Ministry of Education, TEDA Applied Physics Institute and School of Physics, Nankai University, Tianjin 300457, China

[2] Shenzhen Research Institute of Nankai University, Shenzhen 518083, China

*Corresponding author: wuqiang@nankai.edu.cn

**Corresponding author: pancp@nankai.edu.cn

Received February 12, 2023 | Accepted April 23, 2023 | Posted Online August 7, 2023

Compact terahertz (THz) devices, especially for nonlinear THz components, have received more and more attention due to their potential applications in THz nonlinearity-based sensing, communications, and computing devices. However, effective means to enhance, control, and confine the nonlinear harmonics of THz waves remain a great challenge for micro-scale THz nonlinear devices. In this work, we have established a technique for nonlinear harmonic generation of THz waves based on phonon polariton-enhanced giant THz nonlinearity in a 2D-topologically protected valley photonic microcavity. Effective THz harmonic generation has been observed in both noncentrosymmetric and centrosymmetric nonlinear materials. These results can provide a valuable reference for the generation and control of THz high-harmonics, thus developing new nonlinear devices in the THz regime.

Keywords: nonlinear optics; terahertz waves; topological edge states; valley Hall effect.
DOI: 10.3788/COL202321.081901

1. Introduction

Terahertz (THz) technologies and devices have drawn great interest for their extensive applications in communications, signal processing, drug sensing, and nondestructive testing[1–6]. However, the lack of nonlinear THz technologies and devices has been severely limiting the further development of THz-based fingerprint sensing, nonlinear neural networks, and imaging technologies[7–13]. Some investigations on THz frequency based on topological insulators or Weyl semimetals were performed, where the nonlinear susceptibility may be enhanced by the carriers in the topological bands[14,15]. However, in topological photonics, most THz-frequency research does not involve nonlinearity since, for a long time now, THz nonlinearity was considered very weak. After efficient high-harmonic generation (odd-order only) of THz waves was achieved on graphene in 2018[16], researchers realized four-wave mixing (third-order) in topological graphene plasmon systems two years later[17]. In 2021, we found that the THz wave could achieve giant nonlinearity on a $LiNbO_3$ crystal based on phonon polaritons (second-order nonlinearity)[18], which makes it possible to further achieve giant THz nonlinearity on crystal solids. In addition, topological photonics, featuring phenomenal surface states immune to disorder and impurities[19–25], has led to new applications in the microwave, visible light, and THz frequency bands. Introduction of topological photonic systems in the THz regime has achieved THz signal transmission, polarization splitting, polariton edge transmission, and tuning of THz confinement[26–29]. However, due to the low efficiency of the THz nonlinearity, the nonlinear harmonic generation of THz waves, especially in topological systems, is unexplored.

In this work, we have introduced a scheme for the THz harmonic generation in a 2D topological valley polaritonic microcavity. The obtained results suggest that the topological polaritonic microcavity is a good platform for generating and controlling THz harmonics. By employing the finite-difference time-domain (FDTD) method, based on the quantum valley Hall (QVH) system, we have designed a triangular microcavity using two topological valley photonic crystals (VPCs) based on polar crystals. The interface between two VPCs results in a triangular microcavity, as shown schematically in Fig. 1(a). Both centrosymmetric and noncentrosymmetric nonlinear materials, with the nonlinear susceptibility evaluated by nonlinear Huang equations, are selected to study the harmonic generation process. The harmonic waves are further tuned by changing the amplitude of the THz source power.

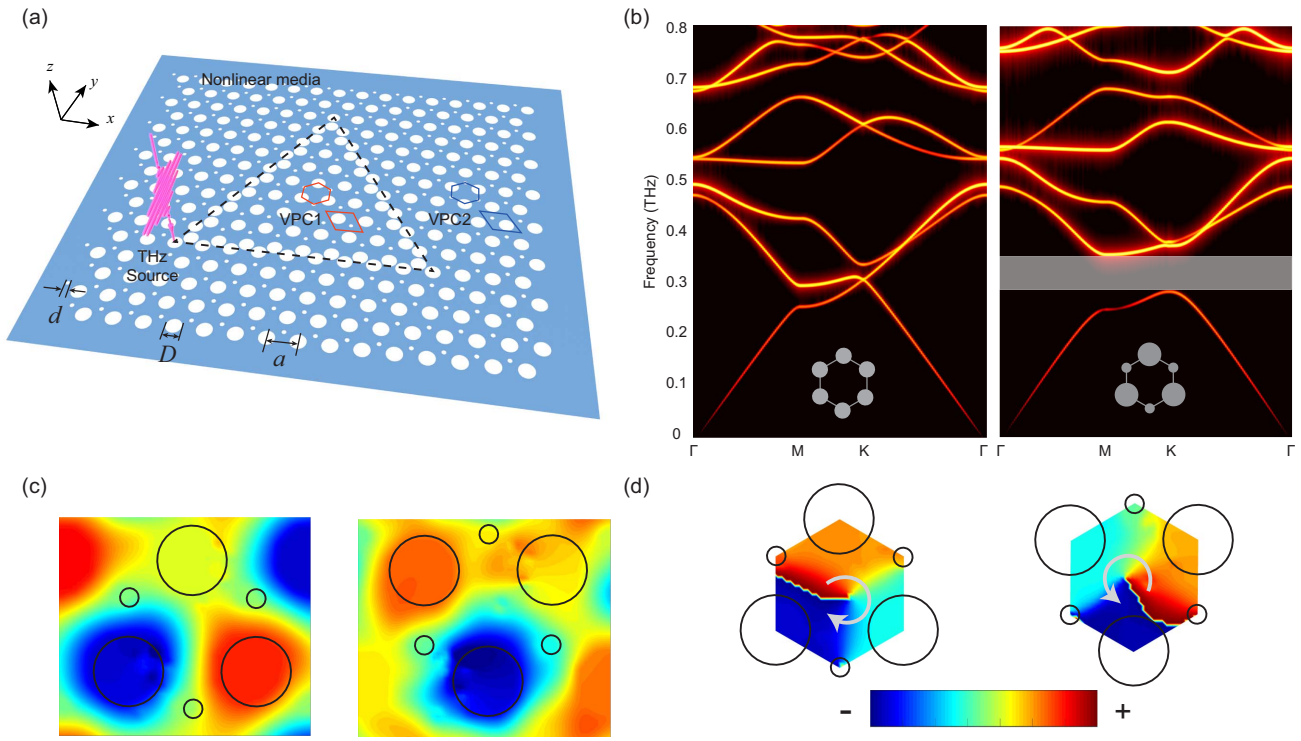

Fig. 1. Design of topological valley polaritonic microcavity and the edge modes. (a) Schematic design of the triangular valley microcavity with air holes etched in a dielectric material of linear susceptibility $\chi^{(1)} = 25$. The triangular topological edge is constructed by two different VPCs, which have different Chern numbers. A *y*-polarized THz source is placed at the left-bottom corner of the triangular microcavity. Lattice parameters are $a = 150$ μm, $D = 80$ μm, and $d = 22.6$ μm. (b) Energy bands of C_6-symmetry photonic crystals (where $D = d = 51.4$ μm) and VPCs in subfigure (a). The C_3-symmetric VPC breaks the Dirac point with a topological gap between 0.30 to 0.36 THz, scaled by the gray region. (c) Magnetic field (H_z) distribution in the two different VPCs. (d) Phase distribution of the H_z field shows different vortices in the two different VPCs.

2. Linear Modes of the Valley Hall Microcavity

In our design, the honeycomb lattice is adopted to deform two different VPCs. For simplicity, a 2D model within a dielectric material with linear susceptibility, $\chi^{(1)} = 25$, is considered, where absorption, dispersion, and nonlinearity are absent. Here, the prototype model is adopted from a $LiNbO_3$ photonic slab, on which air-hole arrays can be fabricated[28]. A triangular microcavity is constructed by the interface between two types of deformed honeycomb-like lattices, as shown in Fig. 1(a), where the lattice constant is $a = 150$ μm and the deformed lattice site diameters are $D = 80$ μm and $d = 22.6$ μm. The undeformed lattice is C_6 symmetric, where $D = d = 51.4$ μm, which shows a Dirac cone at 0.31 THz in the band structure, and K point in the momentum space, as shown in Fig. 1(b). Here, the energy band is calculated along the boundary of the first Brillouin zone using the plane wave expansion method, where the hot-color mapping represents the calculated band $\tilde{E}(\omega, \rightarrow \mathbf{k})$. Upon deforming the honeycomb lattices so that $D \neq d$, the lattice changes to C_3 symmetric with its inversion symmetry broken. Thus, as the degeneracy of the Dirac cones at K/K' points is broken, a bandgap originates in the distorted lattice, which is indicated in Fig. 1(b). Here, we optimized the value of $D - d = 0.38a$ to reach a broad bandgap for further nonlinear applications[30,31].

In our settings, the bandgap of both deformed lattices ranges from 0.30 to 0.36 THz, which is well located in the 6G communication band. In general, the inequivalent lattice deformation results in different topological properties. In Fig. 1(c), we have shown the magnetic field (H_z) distribution in the first band at the K valley for VPC1 and VPC2, where two different modes are depicted. The phase vortex profile of the H_z field at the K valley in the first band is also calculated and given in Fig. 1(d), which shows a clockwise/anticlockwise rotation by a 2π phase around the center of unit cells. This phase vortex indicates a valley pseudospin in the deformed lattice, which is also known as a photonic valley degree of freedom, and is related to a topologically nontrivial phase[28,32]. The different distribution of the field amplitude and phase vortex of H_z suggests a valley-chirality locking property, thus VPC1 and VPC2 are assigned with different Chern numbers at the K/K' valley[28,32].

In the FDTD calculation, a 2D topological valley polaritonic microcavity with $\chi^{(1)} = 25$ is constructed, and a standard perfect-match layer boundary is employed to avoid the influence of the reflected THz waves. In order to clarify the optical properties of the valley edge modes and the microcavity confinement,

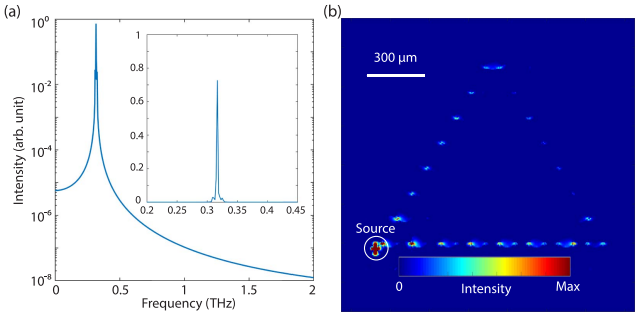

Fig. 2. Linear modes of the topological valley polaritonic microcavity ($\chi^{(1)} = 25$). (a) Mode distribution of the microcavity in the spectrum (logscale). The linear scale is shown in the inset. (b) Intensity distribution of field E_y in the microcavity.

a THz source (dipole source, y-polarized with a center frequency of 0.32 THz) is placed at the left-bottom corner of the triangular microcavity, as depicted in Fig. 1(a). This setting is optimized for the experimental reproduction since the THz waves are generated in the slab as a transverse electric mode[28].

After calculation, a time-resolved field $E_y(x, y, t)$ was obtained. Thus, the spectral information can be obtained through a Fourier transform of $\tilde{E}_y(x, y, \omega) = \int E_y(x, y, t)e^{-i\omega t}\mathrm{d}t$ and $\tilde{E}_y(\omega) = \int \tilde{E}_y(x, y, \omega)\mathrm{d}x\mathrm{d}y$. By calculating the spectrum in the microcavity, an excellent single mode can be seen in the result, which is presented in Fig. 2(a) in logscale, and the linear scale one is also shown in the inset. Further, at 0.32 THz, the E_y field distribution is calculated to obtain the triangular topological valley microcavity mode, as shown in Fig. 2(b). This result is in good agreement with that in the previous research.

3. Harmonic Generation in Noncentrosymmetric Nonlinear Materials

In order to reveal the nonlinear property of the topological edge microcavity and provide a scheme for efficient nonlinear harmonic generation, now we have changed the base materials from linear to nonlinear. Phonon polaritons can assist in giant enhancement of THz nonlinearity. Therefore, a noncentrosymmetric phonon-polariton system is studied with $\chi^{(1)} = 25$, $\chi^{(2)}=10^{-6}$ m/V, where the second-order nonlinear susceptibility is reproduced from our previous results[18].

Employing the similar parameters and the same method as in the linear case, the results in the noncentrosymmetric nonlinear regime can be obtained. As the amplitude of the THz dipole source increases, the nonlinear effects gradually emerge. Figure 3(a) shows the spectra in the triangular microcavity, in which one can notice the gradual growth of nonlinear harmonics as the source power increases. For the source amplitudes smaller than 1×10^4 V/m, no nonlinear signals are observed, as shown by the blue curve in Fig. 3(a). For the source amplitudes 5×10^4 V/m and higher, second-harmonic waves begin to appear, as shown by the red curve. Additionally, third- harmonic

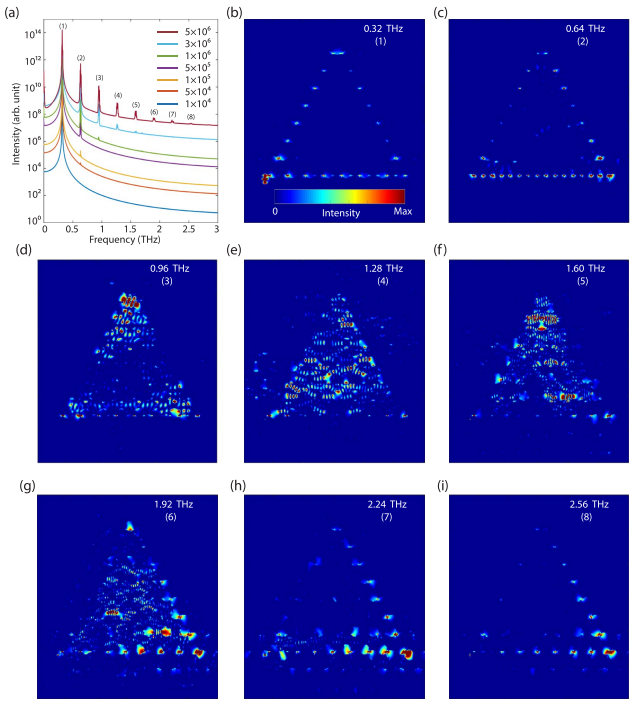

Fig. 3. Nonlinear harmonic generation in the topological valley polaritonic microcavity (noncentrosymmetric materials, $\chi^{(1)} = 25$, $\chi^{(2)} = 10^{-6}$ m/V). (a) Spectra in the microcavity excited by the different source powers (logscale). (b)–(i) E_y intensity distributions for the linear order to 8th-order harmonic waves, respectively (source amplitude is 5×10^6 V/m).

waves are generated as the source amplitude increases to 1×10^6 V/m, as indicated by the green curve. Both the order numbers and the amplitude of the harmonic waves increase further, as the source power gets far stronger. For instance, for the source amplitude 5×10^6 V/m, all the harmonics from the linear order to the 8th-order can be observed in the spectrum. By choosing the source amplitude of 5×10^6 V/m, the mode distributions of the E_y field of all the harmonic modes can be calculated, and the obtained E_y for the linear order to the 8th-order harmonic waves are presented in Figs. 3(b)–3(i). The geometry of the topological microcavity is designed for linear localization, as shown in Fig. 2. When nonlinearity involves, although the linear mode at 0.32 THz is well localized, the high-order harmonics is not located in the topological bandgap [see Fig. 1(b)]. Thus, the high-order harmonics would travel through the whole microcavity after it was generated at the interface.

4. Harmonic Generation in Centrosymmetric Nonlinear Materials

In nonlinear optics and photonics, many nonlinear materials only show odd-order nonlinearity because of their crystal lattice and potential energy being centrosymmetric. In these materials, the most significant contribution to the nonlinearity is the third-order nonlinear susceptibility, $\chi^{(3)}$. In such materials, if the

phonon-polariton system is considered, the pertinent nonlinear susceptibility associated with it can also be evaluated using nonlinear Huang equations as follows[18,33]:

$$\ddot{x} + \gamma\dot{x} + \omega_0^2 x = (Nm)^{-1/2} bE - \beta x^3 + (q/m)E_{\mathrm{ex}},$$
$$P = (Nm)^{1/2} bx + \epsilon_0(\epsilon_\infty - 1)E, \quad (1)$$

where x is the amplitude of motion, ω_0 represents the eigenfrequency of the ions, and γ and β stand for the decay rate and the coefficient of the nonlinear restoring force, respectively. An external driving field E_{ex} is exerted upon the ions whose effective mass and electrical charge are given by m and q, respectively. N shows the oscillator density, whereas E and P indicate the macroscopic electric field and polarization, respectively, in the crystal. The phonon polariton's contribution is characterized by the constant $b = \omega_0\sqrt{\epsilon_0(\epsilon_0 - \epsilon_\infty)}$, with ϵ_0 and ϵ_∞ representing the low- and high-frequency relative permittivity of the material, respectively. The permittivity of the vacuum is $\epsilon_0 = 8.85 \times 10^{-12}$ F/m.

Compared to the nonlinear Huang equations in the noncentrosymmetric materials[18], here the nonlinear restoring force is described by the third-order enharmonic restoring force βx^3 rather than the second order one ax^2. The parameters in Eq. (1) are similar to the previous results, and coefficient $\beta = (\omega_0/d)^2$, where d is the average lattice constant[18,34]. Here, we take parameters from the $LiNbO_3$ crystal, and all the calculation details are similar to the second-order case that can be found in Ref. [18]. Ignoring the evaluation process, the obtained third-order nonlinear susceptibility is about 10^{-13} m^2/V^2. Although the $LiNbO_3$ crystal is noncentrosymmetric, the $\chi^{(3)}$=10^{-13} m^2/V^2 shows a good evaluation of a phonon-polariton polar crystal.

In the FDTD calculation, the nonlinear material is set to be $\chi^{(1)} = 25$ and $\chi^{(3)}$=10^{-13}m^2/V^2, where all other parameters remain identical to the above calculations. In Fig. 4, the results of the nonlinear harmonics in the triangular topological valley microcavity are displayed. For the source amplitudes smaller than 5×10^5 V/m, no nonlinear harmonics are observed. The third-harmonic generation (THG) are produced upon raising the source amplitude to 1×10^6 V/m, as shown in Fig. 4(a).

From the E_y field distribution, obtained at the source amplitude of 3×10^6 V/m, a good edge mode is observed around the triangular microcavity for the linear modes, as shown in Fig. 4(b). However, the mode distribution of the THG waves is shown as a bulk mode rather than as an edge mode around the microcavity, which is displayed in Fig. 4(c). Generally, the field distribution of the topological edge states induced by third harmonics should match with the topological localization pattern[35]. It is worth noting that while the frequency of the topological edge states varied from the middle to the edge in the bandgap, the field distribution of the third harmonics that it induced evolved from the edge states to the bulk states. In this case, field distribution at 0.32 THz presented typical topological edge modes, while the third harmonics that it induced distributed as bulk modes, which is quite beyond our expectation.

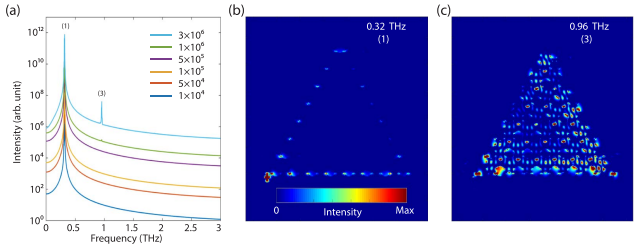

Fig. 4. Nonlinear harmonic generation in the topological valley polaritonic microcavity (centrosymmetric materials, $\chi^{(1)} = 25$, $\chi^{(3)} = 10^{-13}$ m^2/V^2). (a) Spectra in the microcavity excited by the different source powers (logs-cale). (b), (c) E_y intensity distributions of the excited mode and the triple-frequency mode, respectively (source amplitude is 3×10^6 V/m).

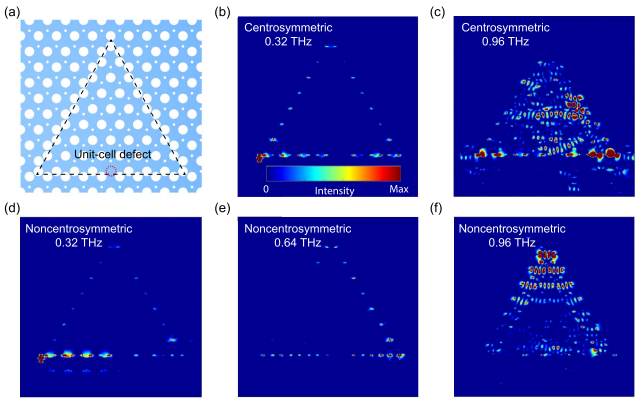

Fig. 5. Topological robust properties against a unit-cell defect. (a) Diagram of the unit-cell defect. (b) and (c) The field distributions of the linear mode and the THG mode against the defect in centrosymmetric nonlinear materials, respectively. (d)–(f) The field distributions of linear, second-order, and third-order modes against the defect, respectively.

Here, we speculate that this is caused by some complicated mechanisms between topological photonics and nonlinear effects. This bulk cavity mode is found to be tunable, which can also be observed in the near-infrared wavelengths[35].

In order to verify the topological robust property, we remove a unit cell from the triangular microcavity in both centrosymmetric and noncentrosymmetric nonlinear materials, as shown in Fig. 5(a). Figure 5(b) shows the topological robust property of the linear mode against this defect, while the THG signal does not maintain a good topological bulk state due to the leaking energy, as seen in Fig. 5(c). For noncentrosymmetric materials, the topological robust was well protected for linear, second-order, and third-order modes against the defect, as indicated in Figs. 5(d)–5(f).

5. Conclusion

In conslusion, we introduced a scheme for the THz harmonic generation in a triangular topological valley polaritonic microcavity, which suggests it to be a good platform for generating and

controlling the THz harmonics. Using the FDTD method, a triangular microcavity is designed using two topological VPCs. Based on the phonon-polariton enhanced nonlinearity using nonlinear Huang equations, we have studied the nonlinear harmonic generation in both noncentrosymmetric and centrosymmetric nonlinear materials. The results have indicated the prominent topological microcavity edge mode of the high-harmonic generation in the noncentrosymmetric nonlinear materials and the bulk topological microcavity mode of third-harmonic waves in the centrosymmetric nonlinear materials. The topological robust properties against defects are also verified. Outcomes of our study can assist as a valuable reference for nonlinear devices, harmonic control, and 6G signal nonlinear processing in the THz regime.

Acknowledgement

This work was supported by the National Natural Science Foundation of China (Nos. 62205158 and 11874229), the China Postdoctoral Science Foundation (No. 2022M711709), the Foundation of State Key Laboratory of Laser Interaction with Matter (No. SKLLIM2101), the 111 Project (No. B23045), and the Program for Changjiang Scholars and Innovative Research Team in University (No. IRT_13R29).

†These authors contributed equally to this work.

References

1. S. Koenig, D. Lopez-Diaz, J. Antes, F. Boes, R. Henneberger, A. Leuther, A. Tessmann, R. Schmogrow, D. Hillerkuss, R. Palmer, T. Zwick, C. Koos, W. Freude, O. Ambacher, J. Leuthold, and I. Kallfass, "Wireless sub-THz communication system with high data rate," Nat. Photonics **7**, 977 (2013).
2. T. Nagatsuma, G. Ducournau, and C. C. Renaud, "Advances in terahertz communications accelerated by photonics," Nat. Photonics **10**, 371 (2016).
3. H. Sarieddeen, M.-S. Alouini, and T. Y. Al-Naffouri, "An overview of signal processing techniques for terahertz communications," Proc. IEEE **109**, 1628 (2021).
4. A. Ahmadivand, B. Gerislioglu, R. Ahuja, and Y. K. Mishra, "Terahertz plasmonics: the rise of toroidal metadevices towards immunobiosensings," Mater. Today **32**, 108 (2020).
5. A. Ren, A. Zahid, D. Fan, X. Yang, M. A. Imran, A. Alomainy, and Q. H. Abbasi, "State-of-the-art in terahertz sensing for food and water security–a comprehensive review," Trends Food Sci. Technol. **85**, 241 (2019).
6. A. G. Davies, A. D. Burnett, W. Fan, E. H. Linfield, and J. E. Cunningham, "Terahertz spectroscopy of explosives and drugs," Mater. Today **11**, 18 (2008).
7. N. Picqué and T. W. Hänsch, "Frequency comb spectroscopy," Nat. Photonics **13**, 146 (2019).
8. W. Peterson, J. G. de Pablo, M. Lindley, K. Hiramatsu, and K. Goda, "Ultrafast impulsive Raman spectroscopy across the terahertz–fingerprint region," Adv. Photonics **4**, 016003 (2022).
9. V. Kilic, M. A. Foster, and J. B. Khurgin, "THz field detection in graphene using deep neural networks," Appl. Phys. Lett. **115**, 161106 (2019).
10. H. Xiong, J. Cai, W. Zhang, and X. Wu, "Silkworm egg development intelligent recognition by THz imaging," in *46th International Conference on Infrared, Millimeter and Terahertz Waves (IRMMW-THz)* (IEEE, 2021), p. 1.
11. J. Naranjo-Torres, M. Mora, R. Hernández-Garca, R. J. Barrientos, C. Fredes, and A. Valenzuela, "A review of convolutional neural network applied to fruit image processing," Appl. Sci. **10**, 3443 (2020).
12. P. Bai, Y. Zhang, T. Wang, Z. Fu, D. Shao, Z. Li, W. Wan, H. Li, J. Cao, X. Guo, and W. Shen, "Broadband THz to NIR up-converter for photon-type THz imaging," Nat. Commun. **10**, 3513 (2019).
13. J. Hou and G. Situ, "Image encryption using spatial nonlinear optics," eLight **2**, 3 (2022).
14. B. Cheng, N. Kanda, T. N. Ikeda, T. Matsuda, P. Xia, T. Schumann, S. Stemmer, J. Itatani, N. Armitage, and R. Matsunaga, "Efficient terahertz harmonic generation with coherent acceleration of electrons in the Dirac semimetal Cd_3AS_2," Phys. Rev. Lett. **124**, 117402 (2020).
15. Z. Dai, M. Manjappa, Y. Yang, T. C. W. Tan, B. Qiang, S. Han, L. J. Wong, F. Xiu, W. Liu, and R. Singh, "High mobility 3D Dirac semimetal (Cd_3AS_2) for ultrafast photoactive terahertz photonics," Adv. Funct. Mater. **31**, 2011011 (2021).
16. H. A. Hafez, S. Kovalev, J.-C. Deinert, Z. Mics, B. Green, N. Awari, M. Chen, S. Germanskiy, U. Lehnert, J. Teichert, Z. Wang, K.-J. Tielrooij, Z. Liu, Z. Chen, A. Narita, K. Müllen, M. Bonn, M. Gensch, and D. Turchinovich, "Extremely efficient terahertz high-harmonic generation in graphene by hot Dirac fermions," Nature **561**, 507 (2018).
17. J. W. You, Z. Lan, and N. C. Panoiu, "Four-wave mixing of topological edge plasmons in graphene metasurfaces," Sci. Adv. **6**, eaaz3910 (2020).
18. Y. Lu, Q. Zhang, Q. Wu, Z. Chen, X. Liu, and J. Xu, "Giant enhancement of THz-frequency optical nonlinearity by phonon polariton in ionic crystals," Nat. Commun. **12**, 3183 (2021).
19. F. D. M. Haldane and S. Raghu, "Possible realization of directional optical waveguides in photonic crystals with broken time-reversal symmetry," Phys. Rev. Lett. **100**, 013904 (2008).
20. Z. Wang, Y. Chong, J. D. Joannopoulos, and M. Soljačić, "Observation of unidirectional backscattering-immune topological electromagnetic states," Nature **461**, 772 (2009).
21. M. C. Rechtsman, J. M. Zeuner, Y. Plotnik, Y. Lumer, D. Podolsky, F. Dreisow, S. Nolte, M. Segev, and A. Szameit, "Photonic floquet topological insulators," Nature **496**, 196 (2013).
22. M. Hafezi, S. Mittal, J. Fan, A. Migdall, and J. M. Taylor, "Imaging topological edge states in silicon photonics," Nat. Photonics **7**, 1001 (2013).
23. A. B. Khanikaev, S. Hossein Mousavi, W.-K. Tse, M. Kargarian, A. H. MacDonald, and G. Shvets, "Photonic topological insulators," Nat. Mater. **12**, 233 (2013).
24. T. Ozawa, H. M. Price, A. Amo, N. Goldman, M. Hafezi, L. Lu, M. C. Rechtsman, D. Schuster, J. Simon, O. Zilberberg, and I. Carusotto, "Topological photonics," Rev. Mod. Phys. **91**, 015006 (2019).
25. Z. Chen and M. Segev, "Highlighting photonics: looking into the next decade," eLight **1**, 2 (2021).
26. Y. Yang, Y. Yamagami, X. Yu, P. Pitchappa, J. Webber, B. Zhang, M. Fujita, T. Nagatsuma, and R. Singh, "Terahertz topological photonics for on-chip communication," Nat. Photonics **14**, 446 (2020).
27. H. Xiong, Q. Wu, Y. Lu, R. Wang, Q. Zhang, J. Qi, J. Yao, and J. Xu, "Polarization-resolved edge states in terahertz topological photonic crystal," Opt. Express **27**, 22819 (2019).
28. H. Xiong, Y. Lu, Q. Wu, Z. Li, J. Qi, X. Xu, R. Ma, and J. Xu, "Topological valley transport of terahertz phonon–polaritons in a $LiNbo_3$ chip," ACS Photonics **8**, 2737 (2021).
29. J. Wang, S. Xia, R. Wang, R. Ma, Y. Lu, X. Zhang, D. Song, Q. Wu, R. Morandotti, J. Xu, and Z. Chen, "Topologically tuned terahertz confinement in a nonlinear photonic chip," Light Sci. Appl. **11**, 1 (2022).
30. S. Jana, K. M. Devi, and D. R. Chowdhury, "Effect of asymmetry on terahertz transmissions in topological photonic crystals comprising of dielectric rod structures," Opt. Commun. **505**, 127589 (2022).
31. S. Jana, K. M. Devi, and D. R. Chowdhury, "Role of unit-cell defects in terahertz topological ring resonators," J. Opt. Soc. Am. B **39**, 1590 (2022).
32. X.-T. He, E.-T. Liang, J.-J. Yuan, H.-Y. Qiu, X.-D. Chen, F.-L. Zhao, and J.-W. Dong, "A silicon-on-insulator slab for topological valley transport," Nat. Commun. **10**, 872 (2019).
33. Y. Lu, Q. Wu, H. Xiong, X. Zhou, Z. Li, J. Qi, X. Xu, R. Ma, J. Fan, Z. Chen, and J. Xu, "Light–matter interaction beyond Born–Oppenheimer approximation mediated by stimulated phonon polaritons," Commun. Phys. **5**, 299 (2022).
34. R. W. Boyd, *Nonlinear Optics*, 3rd ed. (Elsevier, 2008).
35. D. Smirnova, S. Kruk, D. Leykam, E. Melik-Gaykazyan, D.-Y. Choi, and Y. Kivshar, "Third-harmonic generation in photonic topological metasurfaces," Phys. Rev. Lett. **123**, 103901 (2019).